

Orienting the future of bio-macromolecular electron microscopy*

Fei Sun(孙飞)^{1,2,3,†}

¹Center for Biological Imaging, Institute of Biophysics, Chinese Academy of Sciences, Beijing 100101, China

²Center for Excellent, National Laboratory of Biomacromolecule, Institute of Biophysics, Chinese Academy of Sciences, Beijing 100101, China

³School of Life Science, University of Chinese Academy of Sciences, Beijing 101407, China

(Received 4 March 2018; revised manuscript received 2 May 2018; published online 30 May 2018)

With 40 years of development, bio-macromolecule cryo-electron microscopy (cryo-EM) has completed its revolution in terms of resolution and currently plays a highly important role in structural biology study. According to different specimen states, cryo-EM involves three specific techniques: single-particle analysis (SPA), electron tomography and sub-tomogram averaging, and electron diffraction. None of these three techniques have realized their full potential for solving the structures of bio-macromolecules and therefore need additional development. In this review, the current existing bottlenecks of cryo-EM SPA are discussed with theoretical analysis, which include the air–water interface during specimen cryo-vitrification, bio-macromolecular conformational heterogeneity, focus gradient within thick specimens, and electron radiation damage. Furthermore, potential solutions of these bottlenecks worthy of further investigation are proposed and discussed.

Keywords: cryo-electron microscopy, air–water interface, conformational heterogeneity, focus gradient, radiation damage

PACS: 36.20.–r, 68.37.Og, 87.64.Ee, 87.80.–y

DOI: 10.1088/1674-1056/27/6/063601

1. Introduction

Revealing the detailed three-dimensional (3D) structure of bio-macromolecules is one of the important steps in understanding the life. In recent years, cryo-electron microscopy (cryo-EM) has completed its revolution and is becoming one of the major biophysical techniques for studying the 3D structures of bio-macromolecules, especially of membrane protein complexes and supra macromolecular assemblies, thereby having a great impact on our understanding of biology.

The development of cryo-EM technology started in the 1970s and 1980s when significant electron radiation damage to biological specimens was discovered and a low-dose illumination technique was proposed;^[1,2] the cryo-vitrification method to fix the native structure of biological specimens was established;^[3,4] and an image analysis theory for processing low signal-to-noise-ratio (SNR) and low-dose cryo-EM micrographs of bio-macromolecules was developed.^[5] The potential of electron microscopy to determine the high-resolution structure of bio-macromolecules had been revealed in 1975 with the 3D structure of purple membrane^[6] and seriously discussed with a theoretical consideration by Richard Henderson in 1995.^[7] In recent years, with the instrumental advances in electron optics and improved stabilities of electron microscopes, the development of sophisticated image processing software^[8–10] and the automation of data collection,^[11–13] the improvement of phase plate technology,^[14,15] and especially

the success of the direct electron detector (DED),^[16–18] cryo-EM technology has reached its revolution in resolution^[19] with milestone works in which the structure of transient receptor potential cation channel TRPV1 was determined to be 3.4 Å in 2013^[17] and the structure of glutamate dehydrogenase (GDH) was solved to the atomic level in 2016^[20] by cryo-EM. Increasing numbers of supra bio-macromolecular structures, e.g., spliceosome,^[21] photosynthetic complex,^[22] and mitochondrial respiratory complex,^[23] have been solved to the near-atomic level; these could not be achieved by using traditional structural biology approaches.

According to the states of the biological specimen and the experimental workflow, cryo-EM technologies can be classified into three different techniques: cryo-EM single-particle analysis (SPA), cryo-electron tomography (cryo-ET) and sub-tomogram analysis (STA), and cryo-electron diffraction (cryo-ED). Cryo-EM SPA is used to analyze the 3D structure of purified bio-macromolecules in solution, which are cryo-vitrified into a thin ice layer. Tens of thousands of cryo-EM images of the bio-macromolecule are needed to increase the SNR and reconstruct the high-resolution structure.^[24] Cryo-ET can reconstruct the native 3D structure of a local region within a cell or tissue, and the *in situ* structure of bio-macromolecules can be further analyzed by STA.^[25] There is no need to purify bio-macromolecules from cells or tissue, whereas hundreds of tomograms of cryo-lamella of cells or tissue are needed to obtain

*Project supported by the Science Funds from the Chinese Academy of Sciences (Grant Nos. ZDKYYQ20170002 and XDB08030202) and the Science Funds from the Ministry of Science and Technology of China (Grant Nos. 2017YFA0504700 and 2014CB910700).

†Corresponding author. E-mail: feisun@ibp.ac.cn

the high-resolution *in situ* structure of bio-macromolecules. Cryo-ED is a technique for using a cryo-electron microscope to analyze crystallized biological specimens. It collects the electron diffraction data from two-dimensional (2D) crystals or 3D nano-crystals of bio-macromolecules and then solves the high-resolution structures using crystallographic theories. The technique to study 2D crystals was once called electron crystallography,^[26] and the one to study 3D nano-crystals emerged recently and is called micro-electron diffraction.^[27]

Cryo-EM SPA has matured sufficiently in the past decades to become the major approach in current structural biology. The Nobel Prize in chemistry in 2017 was awarded to Jacques Dubochet, Joachim Frank, and Richard Henderson for their great dedicative work in developing the cryo-EM SPA technique. Cryo-ET STA has developed quickly in recent years and will become an important and unique approach to study the *in situ* structure of bio-macromolecules in the future. In this paper, I discuss the current bottlenecks of cryo-EM SPA and present some potential solutions in my personal view.

2. Current technical bottlenecks in cryo-EM SPA

There have been many thorough reviews to describe the technique of cryo-EM SPA, including the theory, workflow, image processing, and applications.^[28–30] In brief, cryo-EM SPA starts from the cryo-vitrification of a bio-macromolecular solution and collects thousands of high-quality cryo-EM mi-

crographs in a high-throughput manner with a limited illumination dose ($20 \text{ e}/\text{\AA}^2 \sim 60 \text{ e}/\text{\AA}^2$ normally), a defined magnification yielding a proper pixel size ($0.8 \text{ \AA}/\text{pixel} \sim 1.5 \text{ \AA}/\text{pixel}$ normally), and a proper defocus range ($0.8 \text{ }\mu\text{m} \sim 3.0 \text{ }\mu\text{m}$). The subsequent image processing includes micrograph correction (motion and distortion correction, dose weighting) and evaluation, contrast transfer function estimation, particle picking and sorting, 2D and 3D classification, orientation refinement and reconstruction, and post-processing (map sharpening). Because the limited illumination dose yields a noisy raw image of the bio-macromolecules embedded in vitreous ice, tens of thousands of particle images are needed to increase the SNR. Thus, the basic assumption behind cryo-EM SPA is that all the analyzed bio-macromolecules should have an identical structure and conformation, which is actually not always true.

Starting from 2013, when the near-atomic structure of TRPV1 was first solved,^[17] the number of bio-macromolecular structures studied by cryo-EM SPA increased quickly. Through 2017, there are already 5541 cryo-EM maps deposited in the electron microscopy database (EMDB, <http://www.ebi.ac.uk/pdbe/emdb>)^[31] whereas there were only 1566 entries in 2012. Most of the deposited maps were obtained by cryo-EM SPA. However, only a small portion of the maps (313/5541) reach a resolution higher than 4 Å and only a few structures can be solved to a resolution higher than 3 Å (Fig. 1); this raises a barrier for cryo-EM SPA to be widely applied in the pharmaceutical industry.

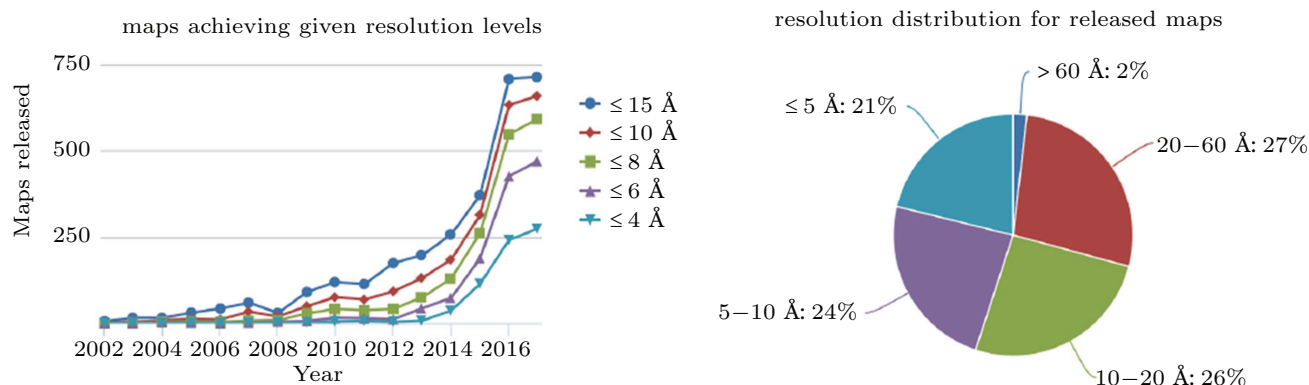


Fig. 1. (color online) Statistics of the electron density maps deposited in the Electron Microscopy Data Bank. The annual numbers of released maps with different reported resolutions are plotted from 2002 to 2017 (left). The distribution of all the released maps through 2017 is statistically plotted vs different resolutions (right). Both panels were generated using the EMDB tool (<http://www.ebi.ac.uk/pdbe/emdb>).

Several bottlenecks still exist in cryo-EM SPA from sample preparation and data collection to image processing, which are impediments to reaching better resolution. In cryo-vitrification during sample preparation, the existence of an air-water interface increases the possibility of disassociation and denaturing of bio-macromolecules, which prevents many fragile macromolecular complexes from study by cryo-EM SPA. The existence of the intrinsic conformational flexibility of bio-macromolecules rules out the basic assumption of the identi-

cal structure and conformation in cryo-EM SPA, which has restricted the approach to high resolution. During cryo-EM imaging, the SNR from the current instrument and hardware is still not sufficient to study the high-resolution 3D structures of bio-macromolecules when their molecular weight is smaller than 60 kDa ($1 \text{ Da} = 1.66054 \times 10^{-27} \text{ kg}$). The phase plate and DED technologies can be improved to better increase the current cryo-EM SNR. The cryo-electron microscope can be made more stable, easy to use, and dedicative for the cryo-

EM SPA workflow with greatly improved throughput. When the size of a bio-macromolecule becomes large or the thickness of the biological material increases, the existence of the Ewald sphere effect and focus gradient limits the approachable resolution of cryo-EM imaging in the current theoretical framework, which needs to be solved in both the experimental and image processing procedures. The ultimate bottleneck of cryo-EM SPA is the physical nature of radiation damage to bio-macromolecules during cryo-EM imaging, which cannot be avoided and is the key limitation to achieving atomic resolution in cryo-EM SPA.

Glaeser provided an excellent discussion of these bottlenecks with thoughtful perspectives.^[32] Here, I focus on cryo-vitrification, conformational heterogeneity, thick samples, and electron radiation damage, further discuss these limitations in theory, and propose new solutions to solve these bottlenecks.

2.1. Cryo-vitrification and the air–water interface

The current cryo-vitrification method was originally invented by Dubochet's group in 1984,^[3] and is called plunge freezing. The EM grid coated with a carbon supporting film is pre-treated with plasma cleaner and then nipped by a fine tweezer and mounted onto the plunge freezer. A small amount ($3\ \mu\text{l}\sim 5\ \mu\text{l}$) of bio-macromolecule solution is dropped onto the supporting film. After a few seconds of incubation, most of the liquid is blotted with filter paper, leaving a thin layer of the solution ($30\ \text{nm}\sim 50\ \text{nm}$ thickness) on the grid. Subsequently, the grid is then quickly plunged into liquid ethane that is pre-cooled by liquid nitrogen, resulting in vitrification of the thin solution layer. Finally, the bio-macromolecules are embedded in the vitreous ice with their native structure preserved. The procedure of this cryo-vitrification method has not changed much since its invention and is still widely used for cryo-EM SPA. Several vendors provide commercialized instruments (Thermo Fisher Vitrobot, Leica EM GP, and Gatan CP3) for cryo-vitrification, which increase the throughput and reproducibility by accurately controlling experimental parameters, such as humidity, temperature, and blotting time.

However, many laboratories have found that the homogeneity of the bio-macromolecule is significantly decreased from the cryo-vitrified sample when compared with the negatively stained sample. The worst case is that although the specimen shows an even distribution with homogenous size and shape from the negative stain electron micrographs, few particles can be identified or recognized from the cryo-EM micrographs (Fig. 2(a)). The reason for this phenomenon has been fully discussed by Glaeser and colleagues^[33,34] and is now widely recognized to be an effect of the air–water interface (Fig. 2(b)).

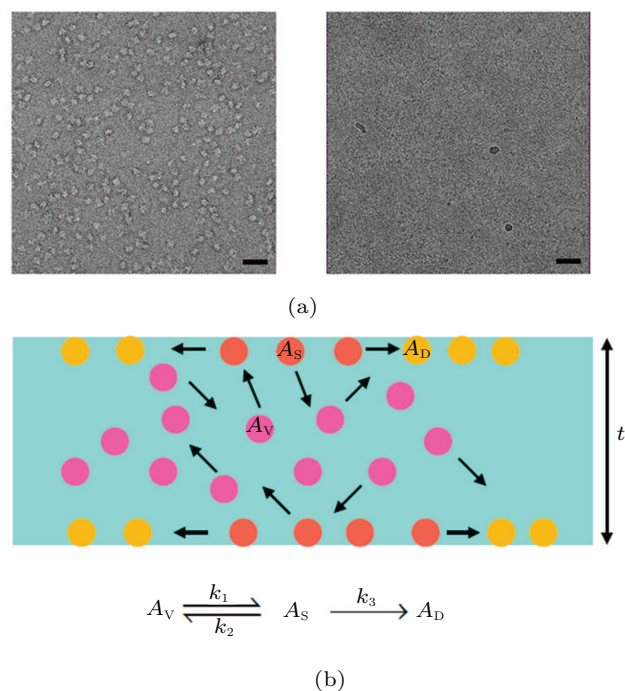


Fig. 2. (color online) Air–water interface effects during specimen cryo-vitrification. (a) The bio-macromolecule specimen exhibits homogenous distribution and good shape in negative electron microscopy (left), but is prone to degradation and is difficult to observe in cryo-electron microscopy (right). Scale bar, 50 nm. (b) Diagram showing the physical process during specimen cryo-vitrification. Bio-macromolecules in their native state (A_V) are colored pink, those absorbed in the air–water interface (A_S) are colored orange, and those denatured (A_D) are in yellow. The thickness (t) of the solution layer after blotting is between 30 nm and 100 nm.

During plunge freezing, the thin solution layer after filter paper blotting results in a very large surface-to-volume ratio ($\sim 20\ \mu\text{m}^{-1}$) in comparison with its original value of ($\sim 0.002\ \mu\text{m}^{-1}$). Thus, the bio-macromolecule in the thin layer of solution has a great opportunity to reach the surface; this has been observed from a recent cryo-ET study where $\sim 90\%$ of particles were absorbed in the air–water interface.^[35] The movement of the bio-macromolecule $\sqrt{x^2}$ follows the Brownian motion law according to

$$\frac{x^2}{t} = \frac{k_B T}{3\pi\eta r}, \quad (1)$$

where t is the time of the motion, r is the radius of the bio-macromolecule, η is the coefficient of viscosity of the solution (for water at $10\ ^\circ\text{C}$, it is $1.308\ \text{mPa}\cdot\text{s}$), k_B is the Boltzmann constant, and T is the temperature in unit K. For a layer thickness of 50 nm and a 20-nm diameter of the bio-macromolecule, the average time (at $T = 283\ \text{K}$) for the bio-macromolecule reaching the surface can be estimated as $\sim 20\ \text{ms}$. The time can be even shorter ($\sim 6\ \text{ms}$) for thinner ice (40-nm thickness) and smaller bio-macromolecules (10-nm diameter). As a result, upon the formation of the thin layer of solution, the bio-macromolecules can quickly approach the air–water interface, which has a great possibility of inducing denaturation of the bio-macromolecule.^[34] The thermodynamics

of this procedure can be further described as (Fig. 2(b))



where A_V represents the bio-macromolecules in the solution, A_S represents the bio-macromolecules bound to the air–water interface, and A_D represents the denatured bio-macromolecules. Thus, the speed of bio-macromolecule denaturation is determined by the reaction constants k_1 , k_2 , and k_3 . A molecular dynamics simulation to study the absorption behavior of lysozyme onto the hydrophobic surface of graphite suggested that the secondary structures of lysozyme disappear at 10 ns after binding to the surface.^[36] Thus, the order of k_3 can be estimated as $1 \times 10^7 \text{ s}^{-1} \sim 1 \times 10^8 \text{ s}^{-1}$, and the denaturation of the bio-macromolecule can occur in less than 1 μs .

During plunge freezing, the time from the completion of blotting to plunging into liquid ethane is normally seconds, which is much longer than that for bio-macromolecules approaching the air–water interface and denaturing. Therefore, it can be explained why it was difficult to obtain good cryo-EM micrographs for those fragile bio-macromolecules that are easily denatured (or dissociated), although they can be well captured in negative stain electron micrographs (Fig. 2(a)).

The existence of the air–water interface has become one of the most important bottlenecks for cryo-EM SPA to obtain high-resolution structures of many bio-macromolecules. To overcome this bottleneck, researchers have developed multiple ways to reduce the air–water interface by utilizing an additional ultrathin ($\sim 2 \text{ nm}$) carbon film^[34] or developing affinity grids.^[37,38] Adding surfactant into the solution could also be useful to form a “cover slip” at the air–water interface and therefore protect the bio-macromolecules from denaturation.^[39] In addition, new instruments using automatic robotics have been recently developed, such as the Spotiton^[40] and “grid writer”,^[41] which avoid paper blotting and can minimize the time between the formation of the thin layer and plunge freezing to $\sim 500 \text{ ms}$, which therefore greatly reduces the possibility of the molecule approaching the surface. In a recent study, the new Spotiton robot was reported and the procedure was optimized to reduce the exposure time in the air–water interface to $100 \text{ ms} \sim 200 \text{ ms}$, which efficiently reduced the number of particles reaching the air–water interface and improved the final reconstructed map.^[42]

According to Eqs. (1) and (2), there are other ways to reduce the effect of the air–water interface. Using a high concentration of bio-macromolecules during vitrification may increase the coefficient of viscosity and thus increase the time to approach the surface. Meanwhile, the high concentration also increases the chance of saturating the air–water interface with the denatured molecules and thus allows enough native molecules to remain in the solution. It should be noted that the high concentration could increase the difficulty in the

subsequent particle picking and image processing. Adding a proper chemical reagent to reduce the interaction between the molecule and the air–water interface would be an alternative approach. In this case, the reaction constant k_1 in Eq. (2) is much smaller than k_2 , and thus a large portion of the molecules are kept in the solution. Using a chemical cross-linker to increase the structural stability of the bio-macromolecules would be an additional way to reduce the denaturing reaction constant k_3 .

2.2. Conformational heterogeneity

Cryo-EM SPA assumes that all the bio-macromolecules analyzed in the electron micrographs have an identical structure and conformation. However, this assumption is not rigorously true in most cases because of the unavoidable thermodynamics of bio-macromolecules and would become much worse when heterogeneities exist in the sample.

There are two kinds of bio-macromolecule heterogeneities: composition heterogeneity and conformational heterogeneity. Composition heterogeneity refers to a specimen composed of a mixture of molecules with different ligand-bound states,^[43] a mixture of macromolecular complexes with different subunit stoichiometry, a mixture of macromolecular assembly with different symmetries, or even in the worst case a mixture of the target molecule and contaminations. Conformational heterogeneity refers to a specimen containing the target bio-macromolecules but in different functional states, and can be further divided into two cases, heterogeneity with discrete conformations^[44] and that with continuous conformations.^[45]

The existence of heterogeneity increases the difficulty in SPA image processing and prevents the realization of high-resolution structures. Composition heterogeneity can be efficiently solved by improving the biochemical preparation procedure, such as more specific affinity chromatography. In addition, recent image processing algorithms have been well developed by applying sophisticated statistical tools, such as principal component analysis,^[46,47] maximum log likelihood,^[48] and the Bayesian method.^[49] Utilizing these advanced image processing tools, we can perform efficient image classification to separate bio-macromolecular particles with different compositions and solve the composition heterogeneity.^[50]

Conformational heterogeneity reflects the functional and thermodynamic nature of bio-macromolecules, which could not be easily improved by conventional biochemical approaches. For the case of discrete conformations, the current image classification algorithms can work quite well if the SNR of the particles is large enough to discriminate the different conformations. However, for the case of continuous conformations, it would be difficult to improve the reconstruction resolution by carrying out 3D classification approaches

unless an incredibly large number of particles is collected. There have been a few image processing approaches developed to try to solve the heterogeneity of continuous conformations, including local optimization refinement,^[51] masked refinement,^[52] multi-body refinement,^[53] particle segmentation on micrograph,^[54] the normal mode method,^[55] and the manifold-embedding method.^[56] When using local optimization or the masked refinement approach, researchers assume that the bio-macromolecular particle can be divided into a number of rigid parts and the relative orientations and positions of different rigid parts contribute to the flexibility of the molecular complex. This assumption works in many cases to improve the resolution of bio-macromolecular flexible modules.^[21] However, the assumption is not always true, and the internal conformational changes of different modules should also be considered in many cases.

The recent proposed normal-mode and manifold-embedding methods would be good solutions to study the intrinsic conformational dynamics of bio-macromolecules directly from the raw cryo-EM images of bio-macromolecular particles. The normal mode method first performs atomization of the cryo-EM map and then calculates various normal modes of clustered pseudo atoms. The specific modes are selected to simulate cryo-EM maps with continuous conformations, which are then compared with the raw cryo-EM images.^[55,57,58] Recently, the normal-mode method was successfully applied to study the structure of a transcription pre-initiation complex.^[59]

The manifold-embedding method maps each projection of a bio-macromolecule into a point of hyperspace ($N \times N$ dimension, where N is the size of the projection image). All the points of the bio-macromolecules with different orientations and conformations build a manifold in this hyperspace. The dimension of this manifold is determined by the degree of freedom of bio-macromolecular motion including rotation (3 freedoms), shift (2 freedoms), and conformational changes (various freedoms). Manifold embedding is a mathematical approach to estimate the degree of freedom of the manifold and decompose these freedoms into different principal coordinates. After decomposition, a specific coordinate can be selected and sorted to reconstruct the conformational changes of bio-macromolecules.^[56,60–62]

A recent published review^[63] discussed various image processing algorithms to solve the conformational heterogeneity, especially the continuous conformation problem. In addition to the image processing approaches, here, I propose another biochemical approach to reduce the conformational heterogeneity of bio-macromolecules.

According to the Boltzmann's distribution law, the number of bio-macromolecules at a specific state, N_c , is proportional to $\exp(-E_c/k_B T)$, where E_c is the Gibbs energy of

the bio-macromolecule in state c , k_B is the Boltzmann constant (8.62×10^{-5} eV/K), and T is the temperature of the bio-macromolecule solution. Suppose the lowest Gibbs energy of the state is E_L (normally this state is called steady state and it is not degenerative, i.e., only one conformation corresponds to this state), and the highest Gibbs energy of the state is E_H (normally this state is degenerative, i.e., multiple conformations correspond to this state); the ratio of numbers of molecules between these two states can be determined as

$$r(T) = \frac{N_L}{N_H} = \exp[(E_H - E_L)/k_B T] = \exp(\Delta E/k_B T). \quad (3)$$

The Gibbs energy difference ΔE between two states of bio-macromolecules is 40 meV \sim 90 meV.^[45,62] Then, the ratio of the numbers can be estimated as $r(298 \text{ K}) = 4.7 \sim 33.2$ (room temperature), $r(277.6 \text{ K}) = 5.3 \sim 43.0$ (4°C), $r(253.6 \text{ K}) = 6.2 \sim 61.4$ (-20°C), and $r(193.6 \text{ K}) = 11.0 \sim 219.9$ (-80°C). Therefore, if we could use a chemical cross-linker to fix the steady state at a low temperature (e.g., -20°C or -80°C) before vitrification, there will be more populations of homogeneous bio-macromolecular particles of the steady state in the cryo-EM images, which provides an alternative approach to solve the conformational heterogeneity. To utilize this approach, we need to add glycerol or other cryoprotectants into the bio-macromolecular solution in order to keep the solution in liquid state at low temperature, so that the thermodynamics equilibrium can be reached. Then, the chemical cross-linker is added to the cooled solution to allow the cross-linking reaction to occur. A good cross-linker needs to be screened and optimized to allow an efficient and fast reaction at low temperatures.

2.3. Thick specimen and focus gradient

The current image processing procedure of cryo-EM SPA assumes that the specimen is thin enough that the dynamic scattering, Ewald sphere, and focus gradient effects can be neglected. For a 300-kV acceleration voltage and 100-nm thickness of a vitrified bio specimen, the dynamic scattering effect can still be neglected because it is smaller than the mean free path (~ 350 nm) of 300-keV electrons for the vitrified bio specimen.^[64] However, the Ewald sphere effect limits the resolution to 3.8 Å according to the formula $\sqrt{t \cdot \lambda / (2 \cdot 0.7)}$, where t is the specimen thickness and $\lambda (= 0.02 \text{ Å})$ is the wavelength of 300-keV electrons.^[65] The 100-nm focus gradient induces a phase error of $\pi/2$ at the resolution of 6.3 Å according to the formula $\Delta\chi = \pi\lambda\Delta Zs^2$, where $\Delta\chi$ is the phase error and ΔZ is the focus gradient.^[66] Thus, when the size of the bio-macromolecule or the vitrified ice is thick, the Ewald sphere, especially the focus gradient, will take effect, and should be corrected to improve the resolution. In cryo-EM, the Ewald sphere and focus gradient effects are combined, and corrections of these two effects are actually equivalent.^[65]

The theory of Ewald sphere correction has been well developed,^[65] and various algorithms have been implemented into different programs and tested with simulated data^[67,68] and recent experimental data.^[69] A recent block-focused algorithm was proposed^[70] and proved efficient to solve the structure of a gigantic herpesvirus capsid (~ 125 nm in diameter) to 3.1 \AA .^[71] The effect of the focus gradient was also carefully discussed recently using simulated data.^[72] Here, I discuss the focus gradient effect in a different way and provide a new approximation to solve and correct this effect.

As shown in Fig. 3, if the thickness of the specimen is D , the underfocus of the proximal side is f_0 , and that of the distal side is $f_0 + D$, then the averaged underfocus of the specimen is $f_a = f_0 + D/2$. For a thin specimen, the final image can be simply formulated as

$$I(x, y) = p(x, y) \otimes PSF(f_a, x, y), \quad (4)$$

where $p(x, y)$ is the projection of the structural density $f(x, y, z)$ of the specimen:

$$p(x, y) = \int_{f_0}^{f_0+D} f(x, y, z) dz \quad (5)$$

and $PSF(f_a, x, y)$ is the point spread function of the objective lens, and is the Fourier transformation of the contrast transfer function:

$$CTF(f_a, s_x, s_y) = \sin \chi(f_a, s) = \sin \left(\frac{\pi}{2} \lambda C_s^3 s^4 - \pi \lambda f_a s^2 \right). \quad (6)$$

For simplicity, here we do not consider astigmatism and amplitude contrast, and therefore $s^2 = s_x^2 + s_y^2$.

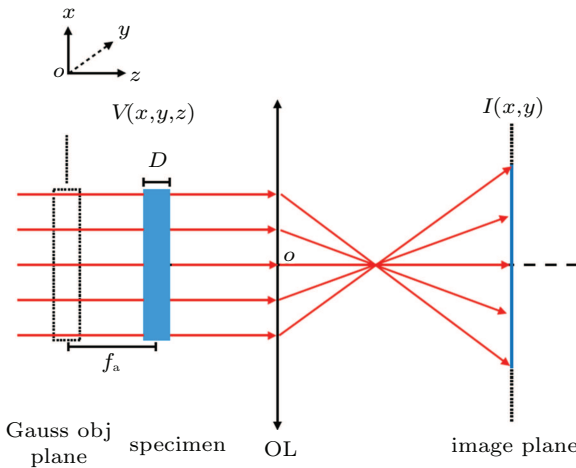


Fig. 3. (color online) Image formation of a thick specimen with average underfocus f_a . Gauss obj plane: the plane where the ideal objective is located according to the Gauss image formation formula. D : the thickness of the specimen. OL: objective lens. $V(x, y, z)$: the density function of the specimen. $I(x, y)$: the image function at the image plane.

However, when the thickness D is large enough, equation (4) must be corrected by dividing the specimen into a series of thin specimens ($n = 0, 1, 2, \dots, N-1$); thus, the final image of a thick specimen can be formulated as

$$I(x, y) = \sum_{n=0}^{N-1} \Delta z \cdot f(x, y, f_0 + n\Delta z) \otimes PSF(f_0 + n\Delta z, x, y). \quad (7)$$

When $N \rightarrow +\infty$, we have

$$\begin{aligned} I(x, y) &= \int_0^D f(x, y, f_0 + z) \otimes PSF(f_0 + z, x, y) dz \\ &= \int_{-D/2}^{D/2} f(x, y, f_a + z) \otimes PSF(f_a + z, x, y) dz. \end{aligned} \quad (8)$$

Considering D (~ 100 nm) $\ll f_a$ (1000 nm \sim 2500 nm), the point spread function can be expanded at $z = 0$ and approximated as

$$PSF(f_a + z, x, y) = PSF(f_a, x, y) + z \cdot \left. \frac{\partial PSF}{\partial z} \right|_{z=0}. \quad (9)$$

Combining Eqs. (8) and (9), we have

$$I(x, y) = I^0(x, y) + I^1(x, y), \quad (10)$$

$$I^0(x, y) = \int_{-D/2}^{D/2} f(x, y, f_a + z) dz \otimes PSF(f_a, x, y), \quad (11)$$

$$I^1(x, y) = \int_{-D/2}^{D/2} f(x, y, f_a + z) z dz \otimes \left. \frac{\partial PSF}{\partial z} \right|_{z=0}. \quad (12)$$

Next, we consider the Fourier transform of the structural density $f(x, y, z)$ of the specimen:

$$\begin{aligned} F(s_x, s_y, s_z) &= \iiint_{z=-D/2}^{D/2} f(x, y, f_a + z) \cdot e^{-i\pi(xs_x + ys_y + zs_z)} dz dx dy. \end{aligned} \quad (13)$$

Thus, we have the projection theorem:

$$\begin{aligned} F(s_x, s_y, 0) &= \iint_{z=-D/2}^{D/2} f(x, y, f_a + z) dz \cdot e^{-i\pi(xs_x + ys_y)} dx dy \\ &= \iint p(x, y) \cdot e^{-i\pi(xs_x + ys_y)} dx dy \end{aligned} \quad (14)$$

and the following relationship:

$$\begin{aligned} \left. \frac{\partial F}{\partial s_z} \right|_{s_z=0} &= \int f(x, y, f_a + z) \cdot e^{-i\pi(xs_x + ys_y + zs_z)} \cdot (-i\pi z) dx dy dz \Big|_{s_z=0} \\ &= \iint \frac{\pi}{i} \int_{z=-D/2}^{D/2} f(x, y, f_a + z) z dz \cdot e^{-i\pi(xs_x + ys_y)} dx dy. \end{aligned} \quad (15)$$

As a result, combining Eqs. (14) and (15) and utilizing the convolution theorem, the Fourier transformation of Eq. (10) becomes

$$\begin{aligned} \hat{I}(s_x, s_y) &= F(s_x, s_y, 0) \cdot CTF(f_a, s) \\ &\quad + \frac{i}{\pi} \left. \frac{\partial F}{\partial s_z} \right|_{s_z=0} \cdot \left. \frac{\partial CTF(f_a + z, s)}{\partial z} \right|_{z=0}. \end{aligned} \quad (16)$$

Combining Eqs. (6) and (16), we have

$$\begin{aligned} \hat{I}(s_x, s_y) &= F(s_x, s_y, 0) \cdot \sin \chi(f_a, s) \\ &\quad - i\lambda \left(\left. \frac{\partial F}{\partial s_z} \right|_{s_z=0} \right) \cdot \cos \chi(f_a, s) \cdot s^2. \end{aligned} \quad (17)$$

From Eq. (17), it is clear that for a thick specimen, the Fourier transform of the cryo-EM image contains an additional term $i\lambda (\partial F / \partial s_z)_{s_z=0} \cdot \cos \chi(f_a, s) \cdot s^2$. This term has a minor contribution at low resolution but will interfere significantly with the first term and induce Thon-ring fading out at high resolution.

Equation (17) provides at least two ways to solve and correct the focus gradient effect. For the first approach, we can take two cryo-EM images of the same specimen with different underfocus, yielding two equations. The underfocus parameters can be accurately estimated by fitting a Thon ring and using the low-resolution data. Then, the structural factor $F(s_x, s_y, 0)$ can be solved directly. The concern of reduced SNR from additional radiation damage of the second exposure has been discussed carefully and can be eliminated.^[65]

The second approach does not need two experimental images, but applies an iterative algorithm to solve the structural factor. Initially, the second term of Eq. (17) is neglected and the normal cryo-EM SPA procedure is performed to obtain the first round of structure. Then, $\partial F / \partial s_z$ can be computed and will be used to update the structural factor $F(s_x, s_y, 0)$ according to Eq. (17). Therefore, the structure of the cryo-EM map can be reconstructed again with improved resolution. This procedure can be iterated several times until convergence is reached.

2.4. Beam-induced motion and radiation damage

Cryo-EM of bio-macromolecules embedded in vitreous ice has suffered from beam-induced motion (BIM) for many years. When accelerated high-energy electrons interact with the specimen, the electrons from the specimen will be scattered and become secondary electrons coming out of the specimen, leaving a positively charged annulus at the illumination area.^[73] This is called the charging effect (“Berriman effect”) from electron beam illumination. Because the thin layer of vitreous ice is an insulator, the positive charges cannot be quickly compensated from the environment and thus induce subsequent physical effects. First, the irregular and metastable structure of the vitrified ice can easily respond to the internal electrostatic repulsion stress from the positive charges and thus result in global mechanical deformation. Such global mechanical deformation is more significant at the beginning of electron illumination^[16] and was observed to have a dome-like shape.^[74] The mechanical deformation of the ice layer during electron illumination results in a blurred cryo-EM image and significantly weakens the high-resolution information. Second, the positively charged annulus induces an additional phase shift of the electron beam, like a microscopic electrostatic lens, which induces additional contrast loss and blurring of the final image,^[73] which, however and fortunately, has a minimal effect on the high resolution cryo-EM SPA technique

according to a recent study.^[75]

In addition to the charging effect that causes BIM, electron beam illumination induces another more severe effect, called radiation damage (or radiolysis). When a secondary electron is ejected, the chemical covalent bond of the molecule is broken, generating many free radicals. The free radicals can migrate quickly and react with the adjacent molecules. As a result, the structure of a bio-macromolecule can be damaged effectively from the electron beam illumination, and the high resolution structural information will be damped significantly when the illumination dose increases.^[2,76] Thus, electron radiation damage must be carefully considered and the electron dose should be carefully controlled for high-resolution cryo-EM SPA work.

The electron radiation damage of vitreous ice-embedded bio-macromolecules further causes a “bubbling” effect that is routinely observed in cryo-EM experiments. Because both water molecules and bio-macromolecules contain abundant hydrogen atoms, electron radiolysis will generate a large amount of hydrogen free radicals, and these hydrogen free radicals subsequently react to form hydrogen molecules.^[77] At the interfaces between bio-macromolecules and ice or the support carbon film and ice, hydrogen molecules frequently accumulate to a high concentration and form a hydrogen gas pocket, which is observed as the “bubbling” effect.^[78] The generation of a hydrogen gas pocket produces additional mechanical stress within the cryo-vitrified specimen and thus becomes another factor of BIM. By using a very low electron radiation dose rate, the accumulation of hydrogen gas can be effectively decreased and thus the “bubbling” effect can be alleviated.^[78] It should be noted that the “bubbling” effect was once developed as a technique to study the internal nucleic structure of viruses.^[79]

Recently, another kind of BIM effect, called beam-induced Brownian motion, was proposed and studied.^[80] This effect describes a pseudo-Brownian motion of vitreous ice embedded bio-macromolecules, which is generated from the beam-induced movement of water molecules. Fortunately, the experimental data and simulation study by Henderson and coworkers suggested that this beam-induced Brownian motion has a minimal effect on the current cryo-EM SPA work unless the bio-macromolecule size is small and the target resolution goes beyond 2 Å.^[80]

The existence of BIM and electron radiation damage has been perceived as the key bottleneck of high resolution cryo-EM SPA for many years until the emergence of DEDs.^[81] The high detective quantum efficiency (DQE) of the DED camera^[82] allows the system to retain the high resolution weak signal under the low-dose electron radiation that is important in reducing radiation damage to the bio-macromolecules. Equally important, the CMOS architecture of the DED cam-

era enables a high frame rate to record a single exposure into a movie, which can be utilized to correct BIM efficiently by applying appropriate image processing algorithms.^[16,74,83] In addition, by using dose fractionation and damage compensation algorithms, the movie mode of the DED camera can further allow use of a high illumination dose for the cryo-EM images to achieve better contrast.^[76]

In addition to the DED, which can correct BIM during the image processing procedure, additional efforts have sought to alleviate the BIM effect; these include spot scan imaging,^[84,85] the paraxial charge compensator,^[86] and development of various supporting films such the cryo-mesh grid, graphene film, and pure gold grid.^[87–89] The pure gold grid was proved to have sufficient mechanical stiffness and good conductivity, which can therefore reduce BIM,^[88] and has been successfully implemented in many high-resolution cryo-EM SPA applications.^[90]

Overall, the efforts in developing the DED, motion correction algorithms, and new types of supporting films in recent years have significantly reduced the effects of BIM and electron radiation damage. Increasing numbers of bio-macromolecular structures are solved to near atomic resolution (3 Å~4 Å) by the cryo-EM SPA approach, in a few cases reaching sub-2-Å resolution.^[20,69] However, the electron radiation damage effect still exists and will become the most important barrier of cryo-EM SPA in the future to achieve atomic resolution. Previous studies showed that the high-resolution (~3 Å) information of vitreous embedded biological specimens starts to fall off after a low dose (3 e/Å²) of electron radiation.^[2] The severe mechanical deformation of the ice layer at the first dose-fractionated frames could not be corrected by image processing algorithms.^[16] As a result, although the first few frames with less radiation damage contain atomic resolution information, this information cannot be restored because of the large BIM, and thus these frames must be discarded in the subsequent image processing.

In the future, there will be two potential ways to further alleviate the electron radiation damage effect. The first possible way is to utilize the quantum entanglement effect of electrons to reduce the shot noise of the electron beam from the normal scale ~ 1/N^{1/2} to the Heisenberg limit ~ 1/N.^[32,91] As a result, we could utilize an even lower electron dose (1 e/Å²) to capture a good image with a sufficient SNR and less radiation damage.^[91] The other possible way is to consider the time scale of the electron radiation damage. If we could take a cryo-EM image before specimen damage occurs, we thus could have an opportunity to obtain a damage-free and high-resolution bio-macromolecule structure. This idea has been proved in the field of serial femtosecond x-ray crystallography with the term of “diffraction before damage”.^[92] In cryo-EM of bio-macromolecules, it is important to estimate

the time scale of specimen damage from electron radiation and then verify the possibility of “imaging before damage.”

For a 300-kV transmission electron microscope, the accelerated electron attains a high velocity

$$v = c \sqrt{1 - \frac{1}{(1 + E/E_0)^2}} = 0.78c = 2.3 \times 10^8 \text{ m/s},$$

where the relativistic effect must be considered; the static energy of an electron is $E_0 = m_0c^2 = 511 \text{ keV}$, the kinetic energy is $E = 300 \text{ keV}$, and the speed of light in vacuum is $c = 3 \times 10^8 \text{ m/s}$. The time for an electron to travel across a specimen with a thickness of $d = 100 \text{ nm}$ is $\Delta t = d/v = 0.33 \text{ fs}$. Thus, we can estimate that the time scale of the interaction between the specimen and a high-energy electron is ~ 1 fs. Many damage events occur in the biological specimen, which can be divided into two processes: the primary damage process and the secondary damage process.^[93,94] The primary damage process includes chemical bond breaking, ionization, and production of secondary electrons and free radicals. Previous studies suggested that the time scale of the primary damage process is 1 ps~10 ps; such damage does not influence the electron microscopic image appreciably,^[95] because the positions of atoms do not change noticeably at this time scale. The only detectable damage in the electron microscopic image occurs in the secondary process, which initiates from the transition of free radicals and includes subsequent cascade reactions induced by free radicals and production of new chemical bonds. During the second process, the positions of atoms in the specimen change significantly, resulting in an appreciable damage effect in the final electron microscopic image. The time scale of the second process depends on the rate of free radical transition, which can be estimated as follows.

As discussed previously, the abundant free radicals generated from vitreous ice-embedded bio-macromolecules are hydrogen free radicals H^* . The transition of H^* follows Fick’s law of diffusion:

$$J = vC = -D \cdot \frac{dC}{dx}, \quad (18)$$

where v is the transition rate of H^* , C is the local concentration of H^* , and the diffusion coefficient can be calculated according to Stokes–Einstein relationship:

$$D = \frac{k_B T}{6\pi\eta r}, \quad (19)$$

where k_B is the Boltzmann constant ($1.38 \times 10^{-23} \text{ J/K}$), T is the temperature of the vitrified specimen, η is the viscosity of the vitreous ice, and r ($\sim 10^{-10} \text{ m}$) is the radius of H^* . Combining Eqs. (18) and (19), we can calculate the transition rate of H^* as

$$v = \frac{1}{C} \cdot \frac{k_B T}{6\pi\eta r} \cdot \frac{dC}{dx}. \quad (20)$$

Suppose, initially, the free radicals H^* are concentrated in a small cubic region with a size of 1 nm^3 ; we could have the following estimate:

$$\frac{1}{C} \cdot \frac{dC}{dx} = \frac{1}{C} \cdot \frac{\Delta C}{\Delta x} \sim \frac{1}{\Delta x} \sim 10^9 \text{ m}^{-1}. \quad (21)$$

Thus, at the temperature ($T = 90 \text{ K}$) of cryo-EM experiments, the transition rate of H^* can be estimated as

$$v \sim \frac{1.38 \times 10^{-23} \times 90}{6 \times 3.14 \times 10^{-3} \times 10^{-10}} \times 10^9 = 0.7 \text{ m/s}. \quad (22)$$

Then, the time for H^* to travel 0.3 nm , the average distance to reach adjacent groups and then undergo radical reaction, can be estimated as

$$\Delta t \sim \frac{0.3 \text{ nm}}{0.7 \text{ m/s}} = 0.4 \text{ ns}. \quad (23)$$

It should be noted that the estimate in Eq. (22) utilizes the water viscosity at room temperature, $\eta_{\text{H}_2\text{O}} = 10^{-3} \text{ Pa}\cdot\text{s}$, where the viscosity of the vitreous ice η_{ice} at 90 K should be much larger (e.g., more than ten times) than the water viscosity at room temperature. Therefore, the time scale for the second damage process is $\sim 10 \text{ ns}$.

This estimate suggests that if we could take a cryo-EM exposure within 10 ns , the appreciable electron radiation damage during the second process can be nearly avoided in the final recorded micrograph. The recently developed ultrafast transmission electron microscopy (UEM)^[96–99] has actually provided an opportunity to test this idea. There are two operating modes of UEM, the stroboscopic mode with picosecond temporal resolution and the single-pulse mode with nanosecond temporal resolution.^[97] The stroboscopic mode is useful for ultrafast electron diffraction experiments and is suitable to study the reversible process of the material. However, the electron radiation damage of bio-macromolecules is irreversible. Thus, to achieve the concept of “imaging before damage,” it is necessary to develop the cryo-ultrafast transmission electron microscopy (cryo-UEM) that is operated in the single-pulse mode. Although there have been some reports of using UEM to observe biological specimens,^[100–102] all these studies were performed in the stroboscopic mode and utilized dehydrated specimens, which should not be relevant to biological functions. There is still a great opportunity to develop and improve single-pulse UEM technology. We are looking forward to the future maturation of cryo-UEM that will bring bio-macromolecular electron microscopy into a new era.

3. Conclusions

Cryo-EM SPA has become the most important technique of bio-macromolecular electron microscopy. The era of studying the structures of bio-macromolecules by using cryo-EM

SPA is only at its beginning. In the near future, we will witness increasing numbers of sophisticated bio-macromolecular complexes whose structures are solved to near-atomic resolution, thus enabling us to gain significant insights to their biological functions. However, as Henderson^[103] and Glaeser^[32] showed, cryo-electron microscopy has not realized its full potential to date. In the future, with better cryo-vitrification techniques to avoid the air–water interface problem, with a better camera and a new type of microscope to further alleviate the electron radiation damage effect, and with some novel image processing algorithms and experimental techniques to solve the focus gradient problem as well as the conformational heterogeneity issue, cryo-EM SPA will expand its full ability to solve the atomic resolution of bio-macromolecules.

Acknowledgements

I would like to apologize that there are also many other pioneer works on developing bio-macromolecular electron microscopy, which are not mentioned in this review because of limited space. I would like to thank Dr. Xiaojun Huang for her critical comments on the manuscript, Shuangbo Zhang for his assistance in literature searching, and Ping Shan and Ruigang Su for their assistance in lab management.

References

- [1] Downing K H 1988 *Ultramicroscopy* **24** 387
- [2] Hayward S B and Glaeser R M 1979 *Ultramicroscopy* **04** 201
- [3] Adrian M, Dubochet J, Lepault J and McDowell A W 1984 *Nature* **308** 32
- [4] Taylor K A and Glaeser R M 1974 *Science* **186** 1036
- [5] Frank J 1990 *Q. Rev. Biophys.* **23** 281
- [6] Henderson R and Unwin P N 1975 *Nature* **257** 28
- [7] Henderson R 1995 *Q. Rev. Biophys.* **28** 171
- [8] Scheres S H 2012 *J. Struct. Biol.* **180** 519
- [9] Grigorieff N 2016 *Methods Enzymol* **579** 191
- [10] Punjani A, Rubinstein J L, Fleet D J and Brubaker M A 2017 *Nature Methods*
- [11] Suloway C, Pulokas J, Fellmann D, Cheng A, Guerra F, Quispe J, Staggs S, Potter C S and Carragher B 2005 *J. Struct. Biol.* **151** 41
- [12] Mastrorade D 2003 *Microscopy and Microanalysis* **9** 1182
- [13] Biyani N, Righetto R D, McLeod R, Caujolle-Bert D, Castano-Diez D, Goldie K N and Stahlberg H 2017 *J. Struct. Biol.* **198** 124
- [14] Khoshouei M, Pfeffer W, Baumeister W, Forster F and Danev R 2016 *J. Struct. Biol.*
- [15] Khoshouei M, Radjainia M, Phillips A J, Gerrard J A, Mitra A K, Plitzko J M, Baumeister W and Danev R 2016 *Nat. Commun.* **7** 10534
- [16] Li X, Mooney P, Zheng S, Booth C R, Braunfeld M B, Gubbens S, Agard D A and Cheng Y 2013 *Nat. Methods*
- [17] Liao M, Cao E, Julius D and Cheng Y 2013 *Nature* **504** 107
- [18] Bai X C, Fernandez I S, McMullan G and Scheres S H 2013 *ELife* **2** e00461
- [19] Kuhlbrandt W 2014 *Science* **343** 1443
- [20] Merk A, Bartesaghi A, Banerjee S, Falconieri V, Rao P, Davis MI, Pragan R, Boxer M B, Earl L A, Milne J L and Subramaniam S 2016 *Cell* **165** 1698
- [21] Yan C, Hang J, Wan R, Huang M, Wong C C and Shi Y 2015 *Science* **349** 1182
- [22] Wei X, Su X, Cao P, Liu X, Chang W, Li M, Zhang X and Liu Z 2016 *Nature* **534** 69
- [23] Vinothkumar K R, Zhu J and Hirst J 2014 *Nature advance online publication*
- [24] Rosenthal P B and Henderson R 2003 *J. Mol. Biol.* **333** 721
- [25] Briggs J A 2013 *Curr. Opin. Struct. Biol.* **23** 261

- [26] Gonen T, Cheng Y, Sliz P, Hiroaki Y, Fujiyoshi Y, Harrison S C and Walz T 2005 *Nature* **438** 633
- [27] Shi D, Nannenga B L, Iadanza M G and Gonen T 2013 *ELife* **2** e01345
- [28] Orlova E V and Saibil H R 2011 *Chem. Rev.* **111** 7710
- [29] Cheng Y 2015 *Cell* **161** 450
- [30] Thompson R F, Walker M, Siebert C A, Muench S P and Ranson N A 2016 *Methods* **100** 3
- [31] Patwardhan A 2017 *Acta Crystallogr D: Struct. Biol.* **73** 503
- [32] Glaeser R M 2016 *Nat. Methods* **13** 28
- [33] Glaeser R M, Han B G, Csencsits R, Killilea A, Pulk A and Cate J H 2016 *Biophys. J.* **110** 749
- [34] Glaeser R M and Han B G 2017 *Biophys. Rep.* **3** 1
- [35] Noble A J, Dandey V P, Wei H, Brasch J, Chase J, Acharya P, Tan Y Z, Zhang Z, Kim L Y, Scapin G, Rapp M, Eng E T, Rice W J, Cheng A, Negro C J, Shapiro L, Kwong P D, Jeruzalmi D, des Georges A, Potter C S and Carragher B 2017 *bioRxiv*
- [36] Raffaini G and Ganazzoli F 2010 *Langmuir* **26** 5679
- [37] Yu G, Li K and Jiang W 2016 *Methods*
- [38] Kelly D F, Dukovski D and Walz T 2010 *J. Mol. Biol.* **400** 675
- [39] Quinn P J and Dawson R M 1970 *Biochem. J.* **116** 671
- [40] Razinkov I, Dandey V, Wei H, Zhang Z, Melnekoff D, Rice W J, Wigge C, Potter C S and Carragher B 2016 *J. Struct. Biol.* **195** 190
- [41] Arnold S A, Albiez S, Bieri A, Syntychaki A, Adaixo R, McLeod R A, Goldie K N, Stahlberg H and Braun T 2017 *J. Struct. Biol.* **197** 220
- [42] Noble A J, Wei H, Dandey V P, Zhang Z, Potter C S and Carragher B 2018 *bioRxiv*
- [43] Scheres S H, Gao H, Valle M, Herman G T, Eggermont P P, Frank J and Carazo J M 2007 *Nat. Methods* **4** 27
- [44] Zhang K, Foster H E, Rondelet A, Lacey S E, Bahi-Buisson N, Bird A W and Carter A P 2017 *Cell* **169** 1303
- [45] Fischer N, Konevega A L, Wintermeyer W, Rodnina M V and Stark H 2010 *Nature* **466** 329
- [46] Van Heel M and Frank J 1981 *Ultramicroscopy* **6** 187
- [47] van Heel M 1984 *Ultramicroscopy* **13** 165
- [48] Sigworth F J, Doerschuk P C, Carazo J M and Scheres S H 2010 *Methods Enzymol* **482** 263
- [49] Scheres S H 2012 *J. Mol. Biol.* **415** 406
- [50] Voorhees R M, Fernandez I S, Scheres S H and Hegde R S 2014 *Cell* **157** 1632
- [51] Shan H, Wang Z, Zhang F, Xiong Y, Yin C C and Sun F 2016 *Protein & cell* **7** 46
- [52] Bai X C, Rajendra E, Yang G, Shi Y and Scheres S H 2015 *ELife* **4**
- [53] Nakane T, Kimanius D, Lindahl E and Scheres S H W 2018 *bioRxiv*
- [54] Zhou Q, Zhou N and Wang H W 2017 *Biophys. Rep.* **3** 43
- [55] Jin Q, Sorzano C O, de la Rosa-Trevin J M, Bilbao-Castro J R, Nunez-Ramirez R, Llorca O, Tama F and Jonic S 2014 *Structure* **22** 496
- [56] Frank J and Ourmazd A 2016 *Methods*
- [57] Sorzano C O, de la Rosa-Trevin J M, Tama F and Jonic S 2014 *J. Struct. Biol.* **188** 134
- [58] Sanchez Sorzano C O, Alvarez-Cabrera A L, Kazemi M, Carazo J M and Jonic S 2016 *Biophys. J.* **110** 1753
- [59] Schilbach S, Hantsche M, Tegunov D, Dienemann C, Wigge C, Urlaub H and Cramer P 2017 *Nature* **551** 204
- [60] Schwander P, Fung R and Ourmazd A 2014 *Philos. Trans. R. Soc. Lond. B Biol. Sci.* **369** 20130567
- [61] Schwander P, Fung R, G. N. Phillips J and Ourmazd A 2010 *New J. Phys.* **12** 035007
- [62] Dashti A, Schwander P, Langlois R, Fung R, Li W, Hosseinizadeh A, Liao H Y, Pallesen J, Sharma G, Stupina V A, Simon A E, Dinman J D, Frank J and Ourmazd A 2014 *Proc. Natl. Acad. Sci. USA* **111** 17492
- [63] Jonic S 2017 *Curr. Opin. Struct. Biol.* **43** 114
- [64] Yan R, Edwards T J, Pankratz L M, Kuhn R J, Lanman J K, Liu J and Jiang W 2015 *J. Struct. Biol.* **192** 287
- [65] DeRosier D J 2000 *Ultramicroscopy* **81** 83
- [66] Zhang K 2016 *J. Struct. Biol.* **93** 1
- [67] Wolf M, DeRosier D J and Grigorieff N 2006 *Ultramicroscopy* **106** 376
- [68] Leong P A, Yu X, Zhou Z H and Jensen G J 2010 *Methods in Enzymology*, ed. Grant J J (Academic Press) pp. 369–380
- [69] Tan Y Z, Aiye S, Mietzsch M, Hull J A, McKenna R, Grieger J, Samulski R J, Baker T S, Agbandje-McKenna M and Lyumkis D 2018 *bioRxiv*
- [70] Zhu D, Wang X, Fang Q, Van Etten J L, Rossmann M G, Rao Z and Zhang X 2018 *Nat. Commun.* **9** 1552
- [71] Yuan S, Wang J, Zhu D, Wang N, Gao Q, Chen W, Tang H, Wang J, Zhang X, Liu H, Rao Z and Wang X 2018 *Science* 360
- [72] Downing K H and Glaeser R M 2017 *Ultramicroscopy* **184** 94
- [73] Brink J, Sherman M B, Berriman J and Chiu W 1998 *Ultramicroscopy* **72** 41
- [74] Brilot A F, Chen J Z, Cheng A, Pan J, Harrison S C, Potter C S, Carragher B, Henderson R and Grigorieff N 2012 *J. Struct. Biol.* **177** 630
- [75] Russo C J and Henderson R 2018 *Ultramicroscopy* **187** 56
- [76] Grant T and Grigorieff N 2015 *ELife* **4** e06980
- [77] Leapman R D and Sun S 1995 *Ultramicroscopy* **59** 71
- [78] Chen J Z, Sachse C, Xu C, Mielke T, Spahn C M and Grigorieff N 2008 *J. Struct. Biol.* **161** 92
- [79] Cheng N, Wu W, Watts N R and Steven A C 2014 *J. Struct. Biol.* **185** 250
- [80] McMullan G, Vinothkumar K R and Henderson R 2015 *Ultramicroscopy* **158** 26
- [81] Jin L, Milazzo A C, Kleinfelder S, Li S, Leblanc P, Duttweiler F, Bouwer J C, Peltier S T, Ellisman M H and Xuong N H 2008 *J. Struct. Biol.* **161** 352
- [82] McMullan G, Faruqi A R, Clare D and Henderson R 2014 *Ultramicroscopy* **147** 156
- [83] Zheng S Q, Palovcak E, Armache J P, Verba K A, Cheng Y and Agard D A 2017 *Nat. Methods* **14** 331
- [84] Bullough P and Henderson R 1987 *Ultramicroscopy* **21** 223
- [85] Downing K H and Glaeser R M 1986 *Ultramicroscopy* **20** 269
- [86] Berriman J A and Rosenthal P B 2012 *Ultramicroscopy* **116** 106
- [87] Russo C J and Passmore L A 2014 *Nat. Methods*
- [88] Russo C J and Passmore L A 2016 *J. Struct. Biol.* **193** 33
- [89] Yoshioka C, Carragher B and Potter C S 2010 *Microsc. Microanal.* **16** 43
- [90] des Georges A, Clarke O B, Zalk R, Yuan Q, Condon K J, Grassucci R A, Hendrickson W A, Marks A R and Frank J 2016 *Cell* **167** 145
- [91] Okamoto H 2012 *Phys. Rev. A* **85** 043810
- [92] Martin-Garcia J M, Conrad C E, Coe J, Roy-Chowdhury S and Fromme P 2016 *Arch. Biochem. Biophys.* **602** 32
- [93] Glaeser R M and Taylor K A 1978 *J. Microscopy* **112** 127
- [94] Hendrickson W A 1976 *J. Mol. Biol.* **106** 889
- [95] Schnabl H 1980 *Ultramicroscopy* **5** 147
- [96] Zewail A H 2010 *Science* **328** 187
- [97] Shorokhov D and Zewail A H 2016 *J. Chem. Phys.* **144** 080901
- [98] Fu X, Chen B, Tang J, Hassan M T and Zewail A H 2017 *Science* **355** 494
- [99] Cao G, Sun S, Li Z, Tian H, Yang H and Li J 2015 *Sci. Rep.* **5** 8404
- [100] Fitzpatrick A W, Lorenz U J, Vanacore G M and Zewail A H 2013 *J. Am. Chem. Soc.* **135** 19123
- [101] Fitzpatrick A W, Park S T and Zewail A H 2013 *Proc. Natl. Acad. Sci. USA* **110** 10976
- [102] Lorenz U J and Zewail A H 2013 *Proc. Natl. Acad. Sci. USA* **110** 2822
- [103] Henderson R 2015 *Arch. Biochem. Biophys.*